Graphene based fully transparent thin film surface acoustic wave devices for sensing and lab-on-chip applications

Jian Zhou[a,*] , Jiangpo Zheng[a,*], Xianglong Shi[b], Zhe Chen[a], Jihui Wu[a], Shuo Xiong[a], Jikui Luo[c], Shurong Dong[d], Hao Jin[d], Huigao Duan[a,z], YongQing Fu[e,z]

[a] State Key Laboratory of Advanced Design and Manufacturing for Vehicle Body, College of Mechanical and Vehicle Engineering, Hunan University, Changsha 410082, P. R. China
[b] Beijing Aerospace Micro-electronics technology Co., 100854, Beijing, P. R. China
[c] Institute of Renewable Energy and Environmental Technologies, Bolton University, Bolton BL3 5AB, United Kingdom
[d] Department of Information Science and Electronic Engineering, Zhejiang University, Hangzhou 310027, P. R. China
[e] Faculty of Engineering and Environment, Northumbria University, Newcastle upon Tyne, NE1 8ST, UK.

[z] E-mail: duanhg@hnu.edu.cn, richard.fu@northumbria.ac.uk
* equal contribution

Abstract: This paper explores to use graphene as transparent interdigital transducer (IDT) electrode for a fully transparent surface acoustic wave (SAW) device due to its extraordinary electrical, physical and mechanical properties. The number of graphene atomic layers was firstly optimized for its best performance as the SAW electrode, and a 4-layered graphene IDT electrode, with aluminum doped zinc oxide, AZO, as the bus bar and wire bonding pad, was selected to fabricate fully transparent ZnO/glass SAW devices. The SAW resonators exhibited obvious resonant response at different wavelengths, and resonance signals with amplitude up to 20 dB were obtained with the transparency above 80%. The graphene-based transparent SAW sensor has been used for different sensing applications. Temperature sensing tests showed that the frequencies increase linearly with the increase of temperature, which has an opposite trend compared to that obtained from a conventional $LiNbO_3$ SAW device. The humidity sensing and human breathing detection have been demonstrated, and discontinuous respiration measurement can be used to distinguish the human respiration at the normal state or the state after exercise. Strong acoustic streaming and particle concentration using the transparent SAW devices have been achieved, which are suitable for microfluidic and lab-on-chip applications.

Keywords: graphene IDTs; transparent SAW; sensors; microfluidics

Introduction

Transparent electronics is one of the emerging technologies with widespread applications and it has unique features of “invisibility” or “transparency”. Owing to this unique property, transparent electronics can be fitted on screens of electronic gadgets/equipment, or on windows of offices and cars etc. to perform various functions such as signal processing, data storage, display, sensing etc., which are normally provided by conventional electronics. This type of transparent electronics will not cause any vision obstruction, thus has great potentials for wide-range applications in con-

sumable electronics, industries, and military activities. To perform proper functions for applications similar to those in the traditional electronics, the transparent electronics requires a range of transparent electronic components and integrated circuits, and indeed many such electronic devices have been explored and developed, including thin-film transistors[1], integrated circuits[2], displays[3], memory[4], sensors[5, 6], solar cells[7], and optoelectronic devices[8]. However, there is a long way to go before the transparent electronics can be utilized for proper and broad applications, not only because the performance and reliability of the components and circuits are needed to improve significantly, but also because it requires various new functional transparent circuits and systems.

Surface acoustic wave (SAW) devices have many applications: in radio-frequency (RF) communication including RFIDs, RF filters, frequency duplexers and RF identification[9, 10]; in sensors for physical parameters and biochemical reaction measurements; in drug development, healthcare, medicine and life sciences with its microfluidics[11-14] and lab-on-a-chip functions[15]. However, there are few studies in developing transparent SAW devices, and it is of great scientific interest to explore if the transparent SAW devices can be successfully developed as it would open the doors for many new applications.

The conventional SAW devices are typically made on piezoelectric bulk materials such as quartz and $LiNbO_3$, or on piezoelectric thin films deposited on solid substrates such as Si and sapphire. They are consisted of a pair of interdigital transducer (IDTs) which are normally made of metals such as Al and Cr/Au with a thickness in the range of 50-200 nm [16], which makes the SAW devices opaque due to either the substrate or visible electrodes. There are significant challenges for making the transparent SAW devices:

(1) Most transparent substrates (e.g. glass) are amorphous, hence it is difficult to deposit high quality, (0002) oriented piezoelectric film on these substrates;

(2) SAW devices generally require thick piezoelectric layers of a few micro-meters (larger than 10% of the SAW wavelength), which easily make the piezoelectric film opaque;

(3) SAW devices require highly conductive IDTs with low resistance for better signal transmission. Transparent conducting oxide materials normally have relatively higher resistivity, and the resistance for the IDTs is usually much higher than the metal counterparts, resulting in poorer device performance;

(4) The material used for SAW IDTs must be transparent to visible light yet have a high conductivity, but it is difficult to increase both transparency and conductivity of the electrode material simultaneously.

Previously, we developed the transparent ZnO SAW devices using aluminum doped ZnO (AZO) as the electrodes on transparent ZnO/glass layer structures with reasonably good performance[17]. However, to achieve low resistance AZO IDTs, the thickness of AZO film should be at least 500 nm, which deteriorates the transmission properties of the SAW devices and performance of the SAW devices due to mass loading effect[9]. In order to further improve the performance, alternative materials are necessary for the transparent SAW devices. Graphene, a two-dimensional (2D) form of carbon atoms with a hexagonal lattice structure, is one of the most promising transparent and conductive materials [18] as it has a high carrier mobility (200000 $cm^2 V^{-1} s^{-1}$), high transmittance (monolayer of 97.7%), excellent thermal stability and conductivity (3000-5000 $W m^{-1} K^{-1}$).[19, 20] In addition, graphene is the thinnest and lightest material, and a monolayer of graphene has a thickness of only ~0.34 nm. It has great potentials for being used as the SAW IDTs, as it has little mass loading effect and is suitable for high frequency application.

In this paper, transparent SAW devices are made using the graphene sheet as the transparent and conductive IDT electrodes on ZnO/glass layered structures. The SAW electrodes are consisted of a composite structure of graphene and AZO (e.g., graphene as IDTs and AZO as bus bar and wire pad) as the graphene is too thin to be used as the wire bonding pads. The device transmission properties are investigated in details, and the SAW devices are further explored for breathe and humidity sensing and for microfluidic applications, in order to demonstrate its unique lab-on-chip applications.

Experimental

Figure 1 presents the schematic illustration of fabrication process of transparent SAW devices. The transparent SAW devices were made on transparent Corning glass substrates (Figure 1a). The ZnO thin films were used as the piezoelectric layers which were deposited using a direct-current (DC) reactive magnetron sputtering system (Figure 1b)). A pure zinc target and an O_2/Ar mixture gas (50/100 sccm) were used during the ZnO deposition. The optimal deposition conditions were found to be:[21] substrate temperature of 100 °C, chamber gas pressure of 2 Pa, DC sputtering power of 200 W and bias voltage of -75 V. After the deposition of ZnO film, the wafer was patterned by photolithography using a negative photoresist to form bus bar and wire pad patterns (Figure 1c). The patterned wafer was then put into the sputtering chamber for deposition of the AZO layer. AZO thin film was deposited by sputtering system using an AZO target (ZnO 98 wt.%: Al_2O_3 2 wt.%,), with the sputtering pressure of 0.3 Pa, the sputtering power of 300 W, and the substrate temperature of 200 °C. Once completed, the wafer was immersed into acetone to remove photoresist /AZO layer except the bus bar and wire pad electrodes (Figure 1d)). After the fabrication of transparent AZO bus bar and wire pad, 4 layers of graphene were transferred onto the ZnO/glass substrate (Figure 1e). Then, a layer of AZ1500 photoresist was spun onto the graphene/ZnO/glass substrate at 4000 rpm for 40 s, baked at 100 °C (60 s), then exposed to UV light (90 mW cm^{-2}). The patterns were then developed in AZ300MIF (2.38%) for 60 s (Figure 1f). For this second UV exposure, it should be aligned well with the first patterns, for the IDTs to be connected with the AZO bus bar. After that, the graphene IDTs were patterned subsequently by etching using an oxygen plasma with the O_2 gas flow rate of 30 sccm, pressure of 1 Pa, power of 50 W and etching time of 30 s (Figure 1g). Then, the photoresist on the graphene IDTs was removed by immersing the sample in acetone and subsequent cleaning in isopropyl alcohol and deionized (DI) water. Finally, the graphene IDTs with AZO wire pad for SAW devices were obtained (Figure 1 h).

The crystalline quality of the layer by layer stacked graphene films was analyzed using Raman spectroscopy (Thermo Scientific DXR) at room temperature with an excitation laser wavelength λ=532 nm and a resolution of 1 cm^{-1}. The surface roughness of the film was characterised using an atomic force microscope (AFM, Agilent 5100) in a contact mode using a Si_3N_4 cantilever. Cross-sectional morphology of the AZO and ZnO films was characterized using a scanning electron microscope (SEM, Hitachi S-4800). Crystalline structure of the AZO and ZnO films was analyzed using X-ray diffraction (XRD, D5000, Siemens) with Cu-kα radiation. The XRD diffraction results obtained from the films were fitted with Voigt functions (i.e., mixed Lorentzian and Gaussian functions) for each kα term[22]. The resistivity of the AZO layer and graphene films were measured by a Van de Paul Hall method.

SAW IDTs have a designed spatial periodicity (e.g., wavelength, λ) of 20, 32 and 40 μm. For the device dimensions, we used 32 μm wavelength of SAW as an example to introduce the details. The total length and width of SAW device (including the AZO wire pad and graphene IDTs) are

about 7.904 mm and 1.224 mm for the device with a wavelength of 32 μm. The width of IDT is 8 μm (1/4 λ) with the metallization ratio of 0.5. Each port of the IDTs has 80 pairs of fingers and 10 reflectors and the aperture is 160 μm (5λ). The distance between the two IDTs is 88 μm (2.75λ). The area of AZO wire pad is about 0.5 mm×0.5 mm with a sufficient large area for wire bonding.

The transmission properties of the devices were measured using an RF vector network analyser (Agilent Technologies, E5061B). Temperature dependence of the transmission properties of the SAW devices as a function of wavelength was measured using a temperature controller, capable of controlling the temperature with an accuracy of 0.1°C. For microfluidic tests, the SAW devices were connected to a signal generator (Agilent Technologies, N9310A), which was amplified by a broadband power amplifier (Amplifier Research, 75A250). The system was carefully impedance-matched to avoid internal reflection of the RF signals. The microfluidic behaviour of de-ionized water droplets was recorded using a video camera.

Results and Discussion

Effects of graphene layers on graphene film properties

SAW devices require high conductive IDTs for the better signal transmission. On the other hand, for the transparent SAW devices, material used for the IDTs must be transparent to visible light. Therefore, the transparency and conductivity of the graphene electrode material need to be optimized for the SAW devices. For this purpose, different layers (1-4 layers) of graphene films were prepared and the properties of graphene films were systematically investigated.

Figure 2a shows the surface morphology and roughness of the graphene film measured by AFM. The root mean square (RMS) roughness data of the samples are 0.56, 0.62, 0.73 and 0.85 nm for the graphene films with layers of 1, 2, 3 and 4, respectively. The RMS roughness increases with the layers of graphene mainly due to the increased wrinkle formation during the repeating transfer process of graphene. Nevertheless, all the surfaces of theses graphene films on SAW devices are very smooth and the RMS roughness of the graphene films is less than 1 nm over a large area of 4×4 μm^2, due to the mono-atomic nature of graphene layer. It should be noted that when the layers of graphene were larger than 4, the graphene were easily peeled off from the layered graphene films, possibly because of the weakened adhesion due to existence of wrinkles. Therefore, in this study, only up to 4 layers of the graphene films were transferred.

Figure 2b shows the effect of graphene layer on the conductivity of the graphene films. With the increase in layer numbers of the graphene from 1 to 4, the sheet resistance values of the graphene layers were measured to be 250, 130.5, 84.6, 77.8 Ω/sq, respectively, i.e., gradually decreasing with increase in layers of the graphene films. Compared with that of the monolayer graphene, the sheet resistance of the 4-layer graphene was decreased by 69%. The sheet resistance of graphene can be expressed using the following equation [23]:

$$Rs = (\sigma N)^{-1}, \quad (1)$$

where σ is the 2D sheet conductivity and N is the number of layers of graphene. In principle, increasing the thickness (e.g., number of layers N) of graphene using the layer-by-layer stacking will decrease the extrinsic sheet resistance, and the experimental results agree well with the theoretical equation calculation (1) as shown in Figure 2b.

Optical transmittance of the graphene films was measured using a UV/visible spectrometer and the transmittance values (for the wavelength of 400~800 nm) of the graphene films were measured to be 97.69%, 95.51%, 92.41%, 90.09% for the graphene layers of 1, 2, 3, 4, respectively, i.e., decreasing linearly with increase in number of graphene layers (Figure 2c). The fitted curve of transmittance of the graphene film can be expressed as T=(100-2.3N), where T is the transmittance

of the graphene film and N the number of graphene layers. The above results reveal that the optical transmittance is reduced by ~2.3% for an additional layer of graphene, due to the increase in the atomic layer thickness of graphene.

The sheet resistance of IDTs has significant effects on the SAW performance. The 4-layer graphene film has the least sheet resistance (77.8 Ω/sq), while still has an optical transmittance over 90% and an RMS roughness less than 1 nm, therefore, we chose 4-layer graphene film to fabricate the SAW IDTs.

Material properties of transparent film layers

Figure 3a shows the fabricated transparent graphene-AZO/ZnO/glass SAW device on a glass wafer, showing its good transparency with the visible background features. Figure 3b is an enlarged image of the transparent graphene-AZO/ZnO/glass SAW device. Optical transmittance results are shown in Figure 3c for the graphene, AZO, ZnO, and AZO/ZnO films. The optical transparency for the 4 layer graphene/glass is about 90.3 %, 89.4% for the AZO layer of 750 nm thickness, 85% for the ZnO layer of 3 μm thickness and 80% for the AZO/ZnO layered film. As the transparency of the graphene IDTs is higher than that of the AZO layer, the transparency for the whole SAW device is mainly determined by layers of AZO/ZnO, i.e. ~80%.

Figure 3d shows the crystalline quality of the layer by layer stacked graphene films (4 layers) analyzed using the Raman spectroscopy. It can be observed the peak position values are at about 1580 cm^{-1} and 2700 cm^{-1} for the 4-layer graphene film, corresponding to its G-band frequency and 2D band frequencies. Figure 3e shows the XRD spectrum of the ZnO film deposited on the glass, and the inset is that of an AZO film. Only (0002) crystal orientation is observed for both the ZnO and AZO films. The full-width at half maximum are 0.168° and 0.304° for the ZnO and AZO films, respectively, corresponding to grain sizes of 61.6 and 28.9 nm based on the Sherrer's equation. Good (0002) orientations and large grain sizes of both the ZnO and AZO are beneficial to obtain a high transparency and low resistivity of AZO films, thus a good performance of the SAW devices. The resistivity and the Hall mobility of the AZO layer measured using the Van de Paul Hall method are ~4×10^{-4} Ω·cm and ~15.6 $cm^2/V\cdot S^{-1}$ respectively, similar to those reported values in literature.[24] Figure 3f shows a cross-section SEM image of AZO wire pad/ZnO/Glass device, in which vertical columnar polycrystalline structure with large grain sizes can be clearly observed for both the ZnO film and AZO layer.

Performance of fully transparent SAW devices

Figure 4 shows the transmission (S_{21}) and reflection (S_{11}) spectra of the transparent graphene-AZO/ZnO/Glass SAW devices with the wavelengths of 40, 32 and 20 μm. The corresponding resonant frequencies, f_r, were found to be 72.3, 88.2 and 136.0 MHz, respectively, as the wavelengths were decreased from 40 to 20 μm. The phase velocities (v_p) of these SAW devices, $v_p = \lambda f$, were calculated to be 2892, 2822.4, and 2720.0 $m\cdot s^{-1}$, respectively, decreasing gradually with decrease in wavelength from 40 μm to 20 μm. The phase velocity for the Rayleigh wave in pure ZnO is ~2650 m/s,[25], whereas that for the Rayleigh wave in glass is 3200 m/s,[26] which is larger than that of ZnO film. When the wavelength is decreased, more energy is confined in the ZnO film, thus resulting in a lower velocity of wave propagation, and leading to a lower velocity of the layered structure, which is consistent with the observation from other reported ZnO/glass SAW devices.[27]

In order to verify the vibration mechanisms of the graphene-AZO/ZnO/Galss structured SAW devices, we have performed simulations for the SAW device using the Finite Element Analysis

(FEA). The FEA has been conducted using the commercial COMSOL 5.3 software in a two-dimensional (2D) piezo plane strain mode to evaluate the SAW propagation properties, such as resonant frequency and wave modes of the graphene based SAW devices. IDTs are periodic in nature, alternatively consisting of positive and negative potentials. Thus, one period of the electrode would be sufficient to illustrate the performance of the SAW resonator (See Figure 5a). As the acoustic wave is excited by the IDTs not the bus bar and wire pad, in the FEA model the period of IDT is only considered graphene. The relationships among stress, strain, electric field, and electric displacement in the stress–charge of a piezoelectric crystal are given by the piezoelectric constructive as:

$$T_{ij} = C_{ijkl}^{E} \cdot S_{kl} - e_{ijk}^{T} \cdot E_k \quad (2)$$

$$D_i = e_{ikl} \cdot S_{kl} - \varepsilon_{ij}^{S} \cdot E_j \quad (3)$$

where, T_{ij} represents the stress vector, C_{ijkl}^{E} is the elasticity matrix (N/m^2), e_{ijk}^{T} is the piezoelectric matrix (C/m^2), E_k is the electric field vector (V/m), ε_{ij}^{S} is the permittivity matrix (F/m), S_{kl} is the strain vector, and D_i is the electrical displacement (C/m^2). In the model, the glass substrate was used with a fixed bottom boundary condition. A free and zero charge/symmetry boundary condition was assigned to the top surface of the piezoelectric ZnO layer. A polarization voltage value of 1 V was assigned to the graphene electrode, while the other graphene electrode was assigned to be ground. The boundary between the ZnO and graphene was assigned to be free and continuous. The two sides of the ZnO and glass substrate were assigned to be periodical boundary conditions. The thickness, Young's modulus, Poisson's ratio and density of the graphene electrode were set to be 2 nm, 1100 GPa, 0.16 and 2.2 g/cm^3, respectively. The glass substrate was fixed at 50 μm thick (1~2 λ, thick enough for simulation, as the acoustic wave only penetrates into the substrate about one wavelength depth) with the Young's modulus, Poisson's ratio and density of 64 GPa, 0.2 and 2.23 g/cm^3 (datasheet of 7740 Pyrex Glass), respectively, while the material constants of the ZnO are from the ref. [28].

Figure 5a shows the model of the transparent SAW device with graphene IDTs, and the results of surface displacements, vibration modes and changes of resonance frequency with a wavelength of 32 μm. The simulated particle vibrations of resonance frequency show that the transparent SAW devices with the graphene IDTs present the Rayleigh wave mode. The obtained resonant frequencies of the devices with different wavelengths are shown in Figure 5b, 5c and 5d, revealing an excellent agreement with the experimental results at the wavelengths of 40, 32, and 20 μm, respectively.

Sensor and microfluidic applications

SAW devices have been utilized as wireless sensors for monitoring temperature, humidity and pressure etc. [29-31], and as actuators for microfluidics and lab-on-a-chip.[32] If the transparent SAW devices can be proven to be useful for high performance sensors and microfluidics, this will open the door for widespread applications for transparent and invisible sensors and lab-on-a-chip applications.

Transparent SAW temperature sensor. The resonant frequencies of the Rayleigh waves of the SAW devices were measured as a function of temperature as shown in Fig. 6. The frequencies increase linearly with the increase of temperature, which has an opposite trend compared to the conventional $LiNbO_3$ SAW devices.[33] This increasingly linear trend is because the glass substrate (80% content of SiO_2) shows a positive temperature coefficients of frequency (TCF, defined as $\Delta f/\Delta T f_0$) for SAW devices, whereas the ZnO film shows a negative TCF[34, 35]. The TCF

values for the fabricated temperature sensors, are 19.8, 24.6 and 27.0 ppm/K, for the wavelengths of 20, 32 and 40 μm, respectively. With the increase of wavelength of the SAW devices, the TCF value increases as more energy is dispersed into the glass substrate, leading to increased positive TCF values of the layered SAW devices.

Figure 7 shows the changes of resonant frequency for the sensor at various temperatures. When the ambient temperature was increased from 80℃ to 100℃ and then decreased back to 80 ℃, the resonance frequency was increased by ~40 kHz and then decreased by ~40 kHz, respectively. Whereas the resonance frequency was shifted by ~80 kHz, as the temperature was changed from 70℃ to 110℃. This is consistent with those shown in Fig. 6, in which the frequency is shifted by ~20 kHz for a temperature change of 10 ℃。

Transparent SAW humidity sensor. ZnO is a hydrophilic material and water molecules can be easily absorbed and adhered onto the ZnO layer of the device. This induces an additional mass on the surface of the device which influences the transmission characteristics and frequency shifts of the SAW device [36, 37] In general, the frequency change, Δf, induced by a loaded mass, Δm, can be expressed as[38]:

$$\Delta f = \frac{-2{f_r}^2 \Delta m}{A(\rho\mu)^{1/2}} \quad (4)$$

where f_r is the resonant frequency, μ and ρ are the shear modulus and the density of the substrate, respectively, A is the sensing area. Generally, the resonant frequency of the sensors changes with the increase of humidity with a nonlinear characteristic for all the sensors tested, similar to those reported in literature.[39] Figures 8a and 8b show the frequency responses of the SAW sensors to humidity with two different wavelengths of 40 μm and 32 μm, respectively. The device with the wavelength of 20 μm has little frequency shift, mainly because of the relatively weak signal amplitude of S_{21} (Figure 4c). The frequency responses to humidity are in an exponential relationship, and thus can be described by the following relationship,

$$\ln(f - f_0) = \mathrm{A}(\mathrm{RH} - RH_0) + \mathrm{B} \quad (5)$$

where f_0 is the initial resonant frequency, RH_0 is the reference relative humidity, A and B are two coefficient constants. The relationship between the log function of frequency shift and relative humidity has an excellent linearity (Figure 8c and 8d, R^2 being 0.9804 and 0.97 for two wavelengths of 32 and 40 μm, respectively). The sensitivity of the humidity sensor is defined as[39]:

$$\mathrm{S} = \frac{\Delta f}{\Delta RH} \quad (6)$$

where Δf and ΔRH are the frequency shifts and relative humidity changes, respectively. From Equation 6, the average humidity sensitivity of the sensors can be calculated to be 1.83 kHz/%RH and 1.05 kHz/%RH for the wavelengths of 32 and 40 μm, respectively. The results are compatible with those of the other ZnO based SAW devices.[39] The humidity sensitivity of the sensors with a wavelength of 32 μm was higher than that of 40 μm, because the higher the resonant frequency is, the larger frequency shift will be as shown in Equation 4.

To evaluate the repeatability of the sensing characteristics, the time-dependent frequency changes in the humidity sensor were monitored in response to five cycles of exposure to humid air from 18% to 83% relative humidity (Figure 9). The device possesses good repeatability and stability for the frequency changes of the device in five cycles of exposure to the same value of relative humidity. The resonant frequency was returned to its original value when the humidity was decreased from 83% RH to 18% RH without any saturation.

Transparent Human Breath Sensor. Breath monitoring can be used for the early detection of sudden infant death syndrome (SIDS) in sleeping infants, alerting parents to any potential problems.[40], or for monitoring conditions of obstructive sleep apnea of adults. For breath detection, the sensor was placed near the nose and responded to the changes in temperature and humidity during respiration (Figure 10a). Figures 10b to 10 d show the resonant frequencies of the transparent SAW sensors under a discontinuous respiration as a function of time at two conditions: normal state; and the state after exercise. The resonant frequency of the sensor was shifted downwards when it received expiratory air due to the change in humidity (as the temperature was changed from ~25.6℃ to ~28 ℃), and the resonant frequency was recovered to its original value when the volunteer inhaled. The volunteer's normal respiratory rate detected by the transparent SAW sensor was about 16 min^{-1}, which is within the range of respiratory rates of a healthy adult.[39] The shift of the resonant frequency of the transparent SAW sensor caused by expiratory air was about 0.072 MHz (corresponding to the RH change of 24.5%). The response and recovery times of the transparent SAW sensor were about 1.7 s and 0.8 s, respectively (Figure 10e). The total response time for one cycle was about 2.5 s, shorter than the breathing period of ~3.75 s. Therefore, the transparent SAW sensor can be fully recovered before the next breath. These results are much better than the reported results from the conventional metal electrode based SAW devices (2.6 s for Al/LiNbO3 SAW and 4.2 s for Al/ZnO/PI SAW devices).[41]

After the volunteer did physical exercises, the respiratory rate detected by the transparent SAW sensor became faster, which was about 18 min^{-1}, and the shift of the resonant frequency of the transparent SAW sensor caused by expiratory air became as large as 0.12 MHz (corresponding the RH change of 33.3% RH), implying that the transparent SAW device could be used to monitor the human breath and then to monitor the human's sport activities. We also detected the humidity changes using the commercial hygrometer during the breathing process and the humidity change was from 43% RH to 76% RH and from 43 % RH to 88 %RH for normal breathing and breathing after exercise, respectively. The SAW signals were changed with the humidity values for the transparent SAW devices, which agrees well with the commercial hygrometer, thus demonstrating a good potential application on humidity sensors for transparent SAW devices.

Microfluidics based on graphene-AZO/ZnO/Galss SAW device. It is well known that SAW devices can be used for sensors, microfluidics and lab-on-a-chip. When a liquid droplet is located on the path of the surface acoustic wave, the SAW will interact with liquid and the acoustic energy is coupled into the liquid, inducing an acoustic streaming effect (Figure 11a). The transparent graphene SAW device developed in this study can deliver the same function. Figure 11b is a snap shot of acoustic streaming induced by the Rayleigh wave from a transparent SAW device with a wavelength of 32 μm, showing a stable streaming with a double vortex pattern, similar to those obtained from the visible SAW devices on $LiNbO_3$ substrates.[32, 42] Figure 11c shows the measured streaming velocities at the centre of the droplet as a function of RF signal power. The streaming velocity was found to increase with the increase of RF signal voltage applied to the IDT electrode, and reached 2.1cm s^{-1} at a signal power of 1.6 W and droplet size of 2 μL. When the droplet containing TiO_2 nano-particles was positioned off the central line of the wave path, the SAW caused a circulating streaming pattern inside the droplet, thus generating a shear force which pushes particles towards the center of the droplet (Figure 11d). Figure 11e shows the experimental results of concentration effect in the droplet after an RF signal power of 1.6 W was applied with a droplet size of 2 μL. These double vortex streaming and circulating streaming demonstrate that the graphene based transparent SAW devices can be used for transparent microfluidic and lab-on-chip applications.

Conclusion

In summary, we have demonstrated high performance transparent SAW resonators on ZnO/glass substrates using graphene-based composite electrodes. Different layers of graphene films were made and their influences on the graphene characteristics were systematically evaluated. A 4-layered graphene IDT electrode was selected to fabricate the fully transparent ZnO/glass SAW devices. The SAW resonators exhibited resonant response with signal amplitudes up to 20 dB, and the transparency of the SAW devices is above 80%. Experimental and theoretical studies showed that with the decrease in wavelength, the velocity of the layered-structure SAW devices decreases because much more energy is dispersed in the ZnO film, which has a lower velocity of wave propagation compared to the glass substrate. Temperature sensing showed that the resonant frequency increases linearly with the increase of temperature, which has an opposite trend compared to the conventional $LiNbO_3$ SAW devices, and the TCF values for the fabricated SAW temperature sensors are ~19.8 ,~24.6 and 27.0 ppm/K, with wavelengths of 20, 32 and 40 μm. The humidity sensing and human breathing detection have been demonstrated, and discontinuous respiration measurement can be used to distinguish the human respiration at the normal state or the state after exercise. Strong acoustic streaming and particle concentration using the transparent SAW devices have been achieved, and the streaming velocity reached 2.1cm s^{-1} at a signal power of 1.6 W and droplet size of 2 μL. Theses sensing and microfluidic testing results using the transparent SAW devices demonstrate their great potentials for applications in transparent electronics and MEMS devices.

Acknowledgment:

This work was supported by the National Natural Science Foundation of China (No. 51605485), Y.Q. Fu would like to thank the UK Engineering and Physical Sciences Research Council (EPSRC) for support under grant EP/P018998/1, Newton Mobility Grant (IE161019) through Royal Society.

References:

[1] J.L. Zhang, C. Wang, C.W. Zhou, *ACS Nano*, **6,** 7412-7419 (2012).

[2] S. Mandal, G. Dell'Erba, A. Luzio, S.G. Bucella, A. Perinot, A. Calloni, G. Berti, G. Bussetti, L. Duò, A. Facchetti, *Org. Electron.*, **20,**132-141(2015).

[3] C.W. Hsu, B. Zhen, W. Qiu, O. Shapira, B.G. Delacy, J.D. Joannopoulos, M. Soljacic, *Nat. Commun.*, **5,**1-2 (2014).

[4] C.H. Ho, J.R.D. Retamal, P.K. Yang, C.P. Lee, M.L. Tsai, C.F. Kang, J.H. He, *Sci. Rep.*, **7,** 44429(2017).

[5] S.H. Shin, S. Ji, S. Choi, K.H. Pyo, A.B. Wan, J. Park, J. Kim, J.Y. Kim, K.S. Lee, S.Y. Kwon, *Nat. Commun.*, **8,** 14950(2017).

[6] S. Lee, A. Reuveny, J. Reeder, S. Lee, H. Jin, Q. Liu, T. Yokota, T. Sekitani, T. Isoyama, Y. Abe, *Nat. Nanotechnol.*, **11,** 472(2016).

[7] R. Betancur, P. Romerogomez, A. Martinezotero, X. Elias, M. Maymó, J. Martorell, *Nat. Photonics*, 7 (2013) 995-1000.

[8] J. Yun, Ultrathin Metal films for Transparent Electrodes of Flexible Optoelectronic Devices, *Adv. Funct. Mater.*, **27,** 1606641(2017).
[9] C.S. Wang L, Zhang J, et al. , *Appl. Phys. Lett.*, **111,** 253502(2017).
[10] V.P. Plessky, L.M. Reindl, *IEEE Trans. Ultrason. Ferr. Freq. Control.*, **57,** 654-668(2010).
[11] Y.Q. Fu, J.K. Luo, X.Y. Du, A.J. Flewitt, Y. Li, G.H. Markx, A.J. Walton, W.I. Milne, *Sens. Actuators B,* **143,** 606-619 (2010).
[12] C. Devendran, D.J. Collins, A. Ye, A. Neild, *Phys. Rev. Lett*, **118,** 154501 (2017).
[13] L.Y. Yeo, J.R. Friend, *Annu. Rev. Fluid. Mech.*, **46,** 379-406(2014).
[14] G. Destgeer, H.J. Sung, *Lab Chip*, **15,** 2722-2738(2015).
[15] Y.Q. Fu, J.K. Luo, N.T. Nguyen, A.J. Walton, A.J. Flewitt, X.T. Zu, Y. Li, G. Mchale, A. Matthews, E. Iborra, *Prog. Mater Sci.*, **89,** 31-91(2017).
[16] J. Zhou, H.F. Pang, L. Garcia-Gancedo, E. Iborra, M. Clement, M.D. Miguel-Ramos, H. Jin, J.K. Luo, S. Smith, S.R. Dong, *Microfluid. Nanofluid.*, **18,** 537-548(2015).
[17] J. Zhou, X.L. He, W.B. Wang, Q. Zhu, W.P. Xuan, H. Jin, S.R. Dong, D.M. Wang, J.K. Luo, *IEEE Electron Device Lett.*, **34,** 1319-1321(2013).
[18] X. Huang, Z. Zeng, Z. Fan, J. Liu, H. Zhang, *Adv. Mater.*, **24,** 5979-6004(2012).
[19] S. Bae, H. Kim, Y. Lee, X. Xu, J.S. Park, Y. Zheng, J. Balakrishnan, T. Lei, H.R. Kim, Y.I. Song, *Nat. Nanotechnol.*, **5,** 574(2010).
[20] H. Jang, Y.J. Park, X. Chen, T. Das, M.S. Kim, J.H. Ahn, *Adv. Mater.*, **28,** 4184-4202 (2016).
[21] J. Zhou, X. He, H. Jin, W. Wang, B. Feng, S. Dong, D. Wang, G. Zou, J.K.Luo, *J. Appl. Phys.*, **114,** 044502(2013).
[22] T.H. De Keijser, J. Langford, E.J. Mittemeijer, A. Vogels, *J. Appl. Cryst.*, **15,** 308-314(1982).
[23] Y. Wang, S.W. Tong, X.F. Xu, B. Ozyilmaz, K.P. Loh, *Adv. Mater.*, **23,** 1514-1518(2011).
[24] W.T. Yen, Y.C. Lin, J.H. Ke, *Appl. Surf. Sci.*, **257,** 960-968(2010).
[25] K. Kalantar-Zadeh, Y.Y. Chen, B.N. Fry, A. Trinchi, W. Wlodarski, *Proc. 2001 IEEE Ultrason. Symposium*, **351,** 353-356(2001).
[26] J. Fraser, Khuri‐Yakub, G. Kino, The design of efficient broadband wedge transducers, *Appl. Phys. Lett.*, **32,** 698-700(1978).
[27] Y. Nakagawa, *Appl. Phys. Lett.*, **31,** 56-57(1977).
[28] L.L. Brizoual, O. Elmazria, S. Zhgoon, A. Soussou, F. Sarry, M.A. Djouadi, *IEEE Trans. Ultrason. Ferroelectr. Freq. Control*, **57,** 1818-1824(2010).
[29] K. Lee, W. Wang, T. Kim, S. Yang, *J. Micromech. Microeng.*, **17,** 515(2007).
[30] R. Fachberger, A. Erlacher, *Procedia Eng.*, **5,** 224-227(2010).
[31] R. Stoney, D. Geraghty, G.E. O'Donnell, *IEEE Sens. J.*, **14,** 722-728(2014).
[32] J. K. Luo, Y.Q. Fu, Y. Li, X. Y. Du, A. J. Flewitt, A. J. Walton, W. I. Milne, *J. Micromech. Micorengng., **19,*** 054001(2009).
[33] X.G. Tian, H. Liu, L.Q. Tao, Y. Yang, H. Jiang, T.L. Ren, *AIP Adv.*, **6,** 992(2016).
[34] P. Defranould, *Electron. Lett.*, **19,** 823-824(1983).
[35] H. Nakahata, A. Hachigo, K. Itakura, S. Fujii, S. Shikata, *Proceedings of the 2000 IEEE/EIA International Frequency Control Symposium and Exhibition*, 315-320 (2000).
[36] X.L. He, D.J. Li, J. Zhou, W.B. Wang, W.P. Xuan, S.R. Dong, H. Jin, J.K. Luo, *J. Mater. Chem. C,* **1,** 6210-6215(2013).
[37] M. Hoummady, A. Campitelli, W. Wlodarski, *Smart Mater. Struct.*, **6,** 647(1997).
[38] G. Korotcenkov, Chemical Sensors: Fundamentals of Sensing Materials, *International Journal of Computer Networks & Communications*, **5,** 65-84(2010).

[39] W. Xuan, M. He, N. Meng, X. He, W. Wang, J. Chen, T. Shi, T. Hasan, Z. Xu, X. Yang, *Sci. Rep.*, **4,** 7206(2014).
[40] T. Yamada, Y. Hayamizu, Y. Yamamoto, Y. Yomogida, A. Izadinajafabadi, D.N. Futaba, K. Hata, *Nat. Nanotechnol.*, **6,** 296(2011).
[41] H. Jin, X. Tao, S. Dong, Y. Qin, L. Yu, J. Luo, M.J. Deen, *J. Micromech. Microeng.*, **27**, 115006(2017).
[42] X.Y. Du, M.E. Swanwick, Y.Q. Fu, J.K. Luo, A.J. Flewitt, D.S. Lee, S. Maeng, W.I. Milne, , *J. Micromech. Microeng.*, **19,** 035016(2009).

Figure Captions

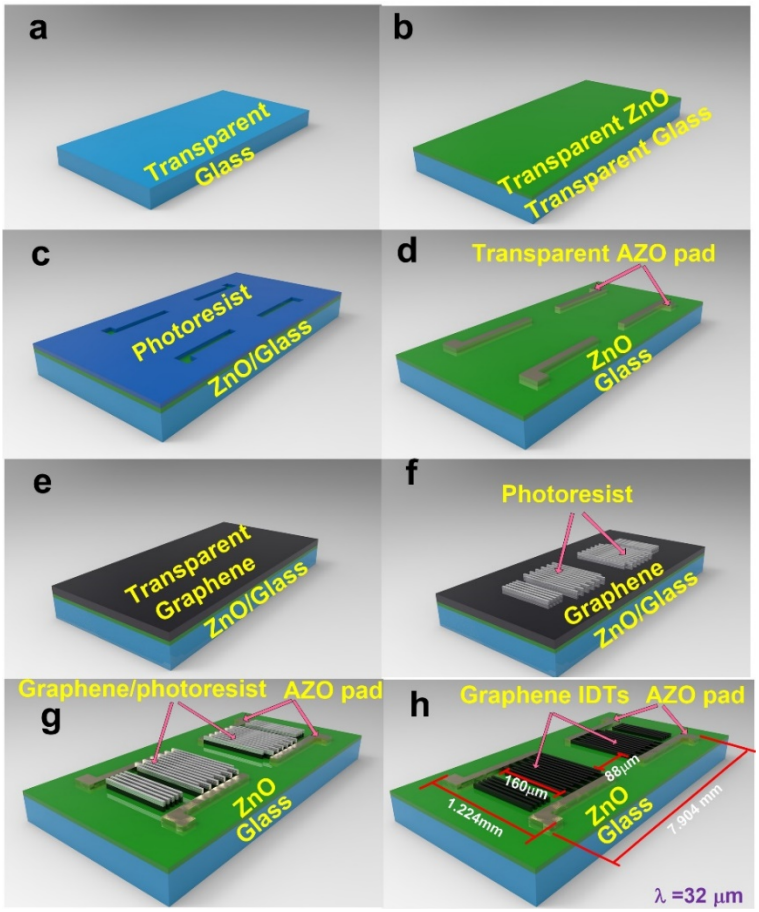

Figure 1. The schematic drawing of fabrication process on the transparent SAW device with novel graphene IDTs. (a)The transparent glass substrate was cleaned and prepared; (b)Depositing the ZnO thin films; (3) Photolithography using a negative photoresist; (4) Depositing the AZO and forming the bus bar and wire pad patterns; (e) Transferring the graphene; (f) photolithography

using a positive photoresist; (g) O_2 plasma etching graphene; (h) Removing the photoresist, subsequent cleaning in isopropyl alcohol and deionized water. Finally, the graphene IDTs with AZO wire pad for SAW devices were obtained (We use 32 μm wavelength of SAW as an example)

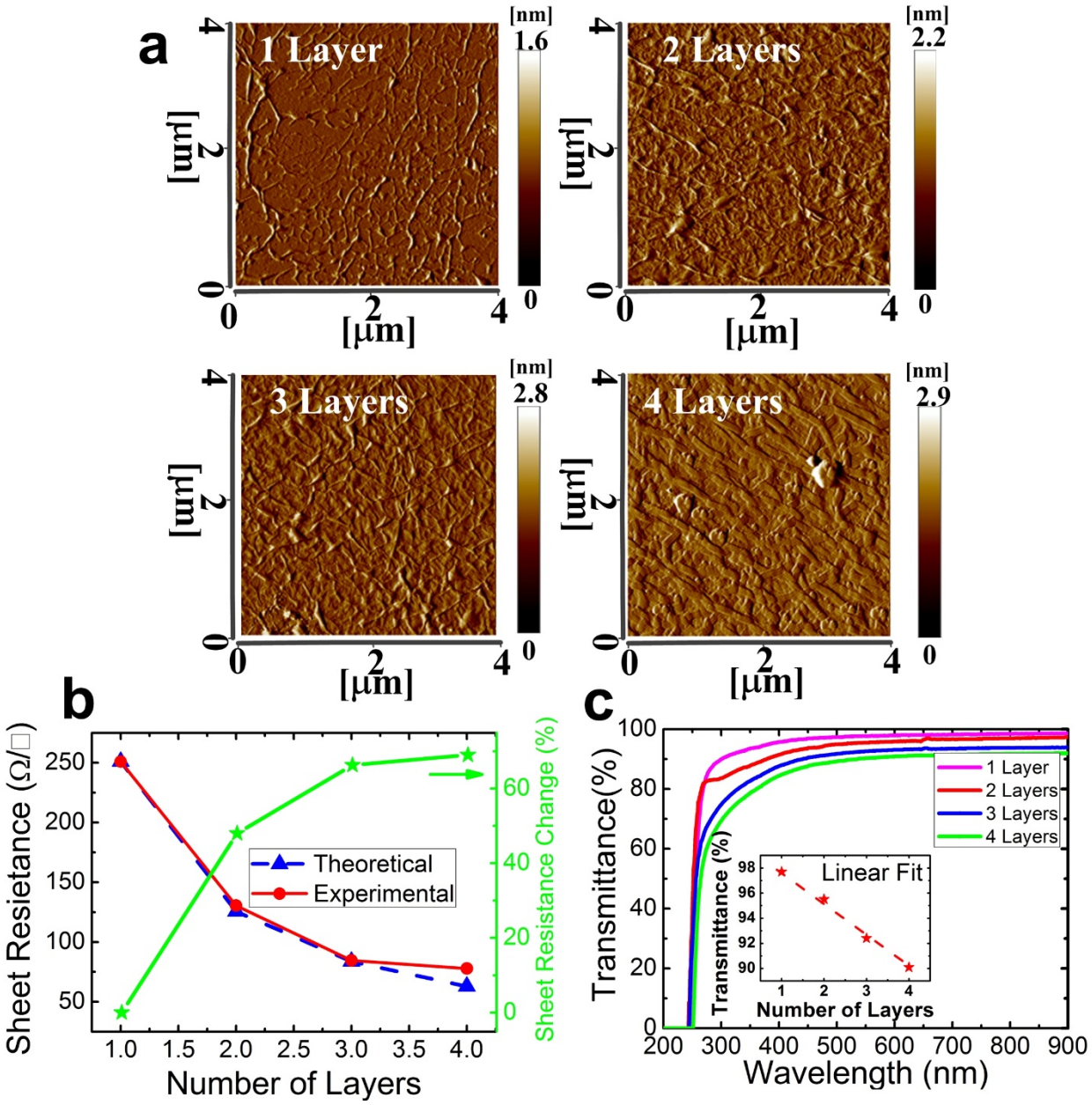

Figure 2. (a) Surface topography of the graphene films as a function of graphene layers by AFM, (b) Resistivity characteristics of the graphene films as a function of graphene layers; (c) UV optical transmittance of the graphene films as a function of graphene layers.

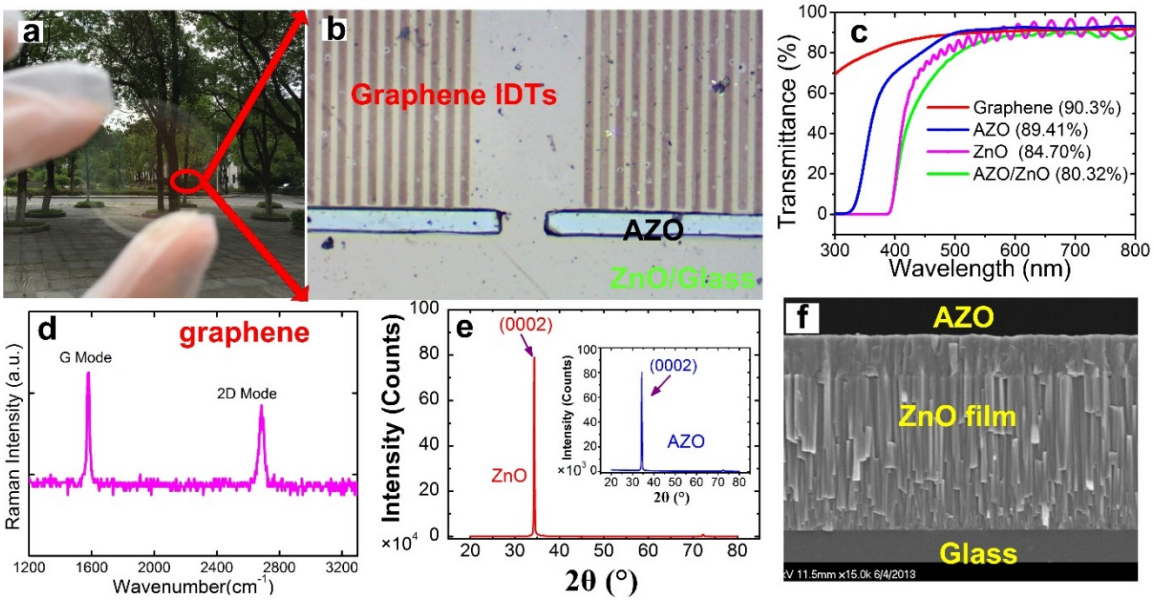

Figure 3. (a) A photograph of a glass wafer with fabricated transparent graphene-AZO/ZnO/Glass SAW devices, showing a good visibility of the back features; (b) a high resolution microscope image of a transparent graphene-AZO/ZnO/Glass SAW devices; (c) Optical transmittance for the graphene (4 layers), AZO, ZnO, and AZO/ZnO films on glass; showing the transmittance above 80%; (d) Raman spectroscopy measurement of graphene films (4 layers); (e) XRD spectrum of the ZnO film and AZO films on the glass; (f) the SEM picture of the ZnO/AZO film.

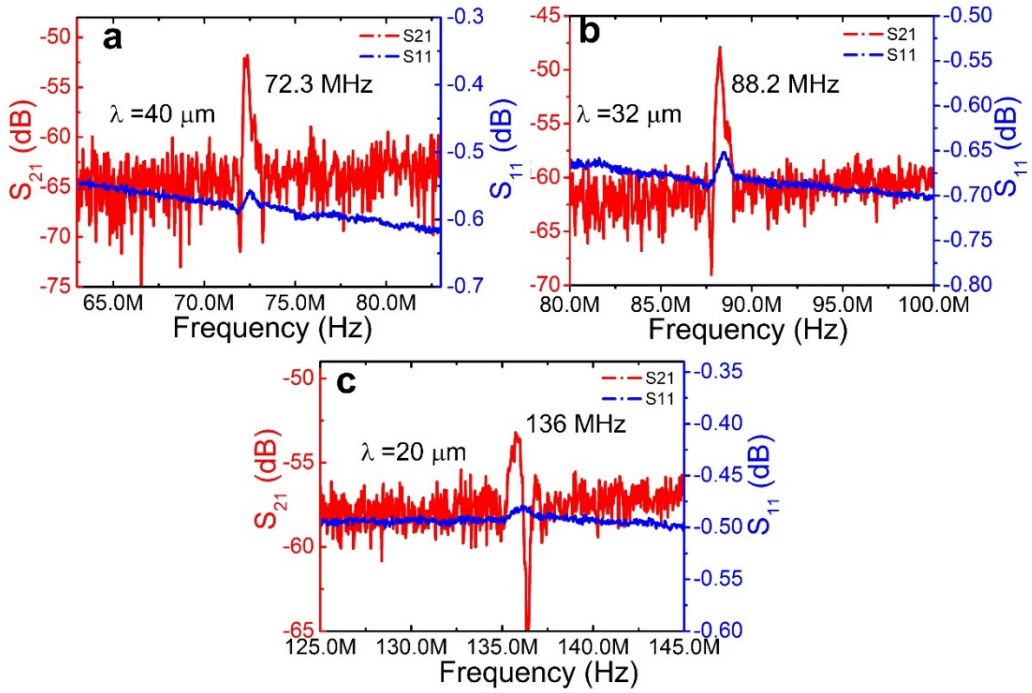

Figure 4. Transmission (S_{21}) and reflection (S_{11}) characteristics spectra of the graphene-AZO/ZnO/Galss structured SAW devices at the wavelength of: (a) 40; (b) 32 and (c) 20 μm.

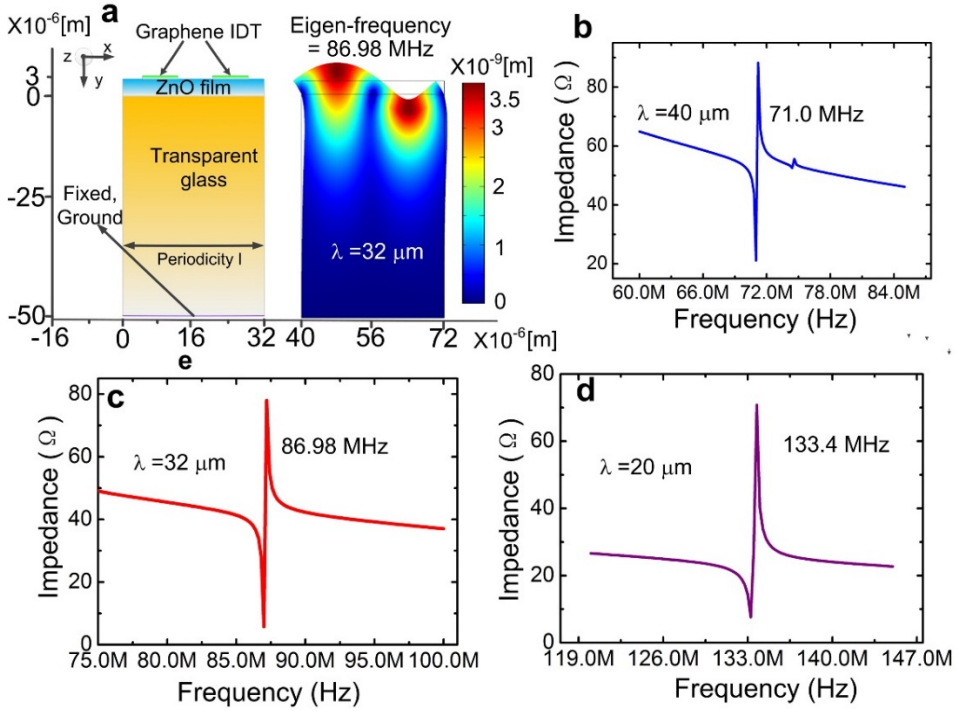

Figure 5. (a) Geometry of a periodic cell in the simulation(left) and results of surface displacements at the resonance frequency with a wavelength of 32 μm(right); (b), (c) and (d) simulated impedance of the graphene-AZO/ZnO/Galss structured SAW devices at the wavelength of 40, 32 and 20 μm, respectively.

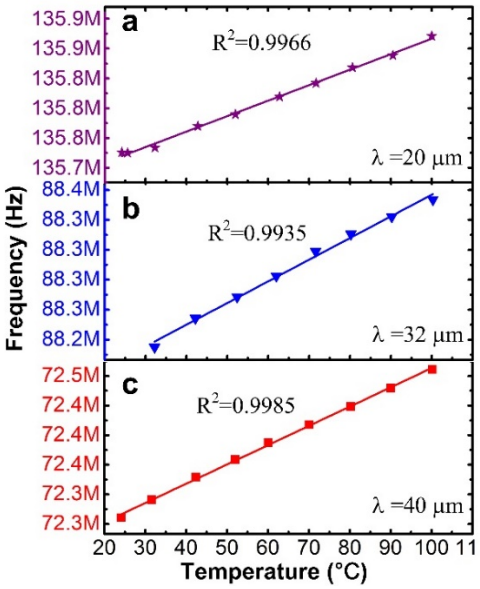

Figure 6. Resonant frequency increases linearly with increase in temperature for the transparent temperature SAW device with a wavelength of (a) 20 μm, (b) 32 μm and (c) 40 μm with the R^2 being 0.9866, 0.9935 and 0.9985 (R^2 is the correlation coefficient).

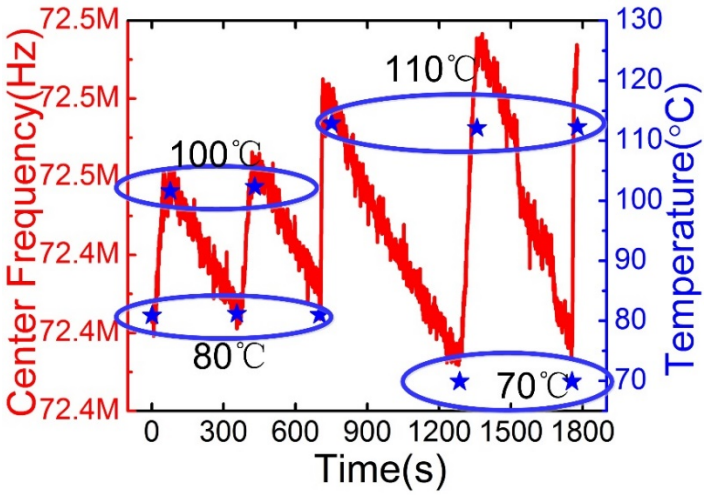

Figure 7. Resonant frequency changes in the transparent temperature sensor under various temperature environments.

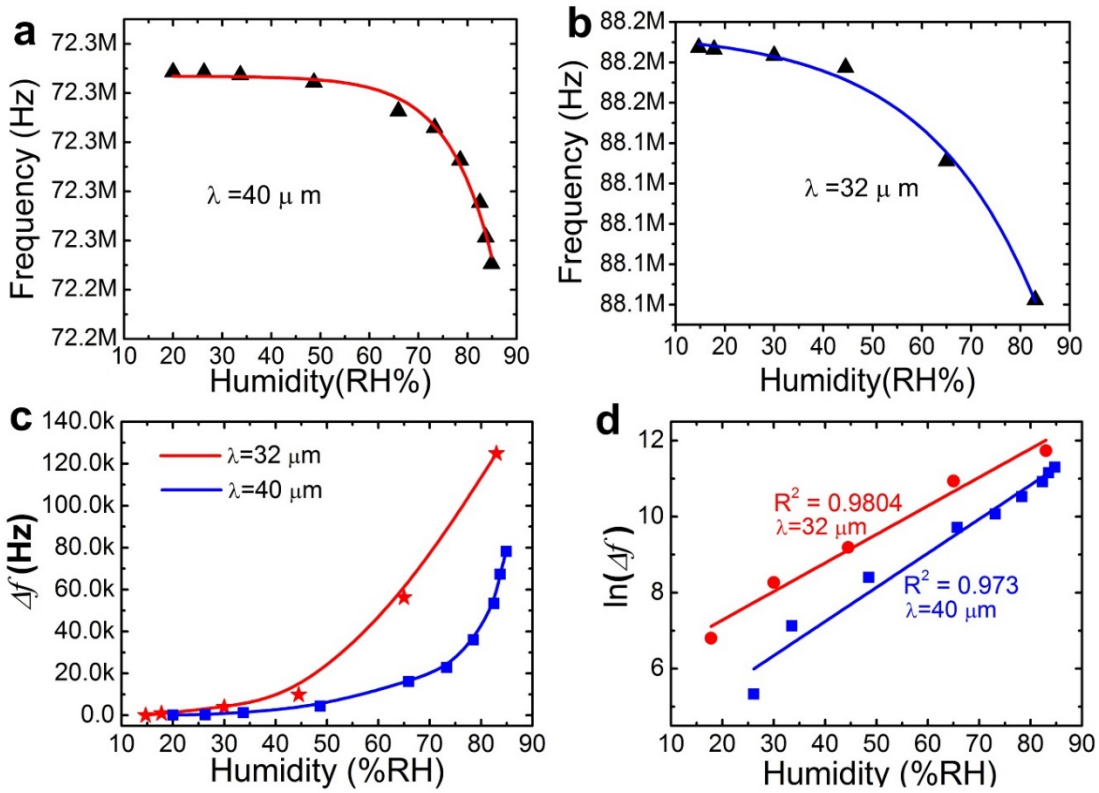

Figure 8. (a)&(b) The resonant frequency shifts as a function of relative humidity for transparent SAW sensors at wavelength of 40 μm and 32 μm, respectively;(c) The frequency shift as a function of humidity for transparent SAW sensors for wavelength of 32 and 40 μm; (d) The change of frequency as an exponential function of relative humidity is found with excellent linearity (R^2 is the correlation coefficient).

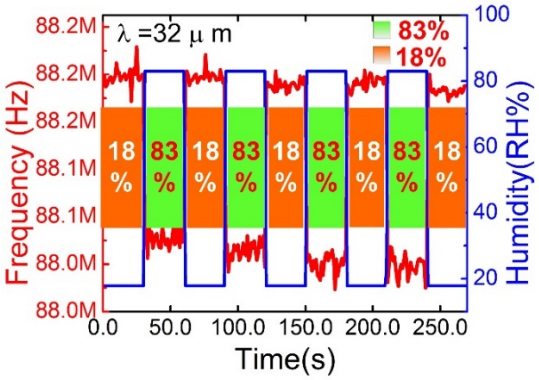

Figure 9. Resonant frequency changes in the transparent SAW humidity sensor after five cycles of exposure to environments with different humidity levels.

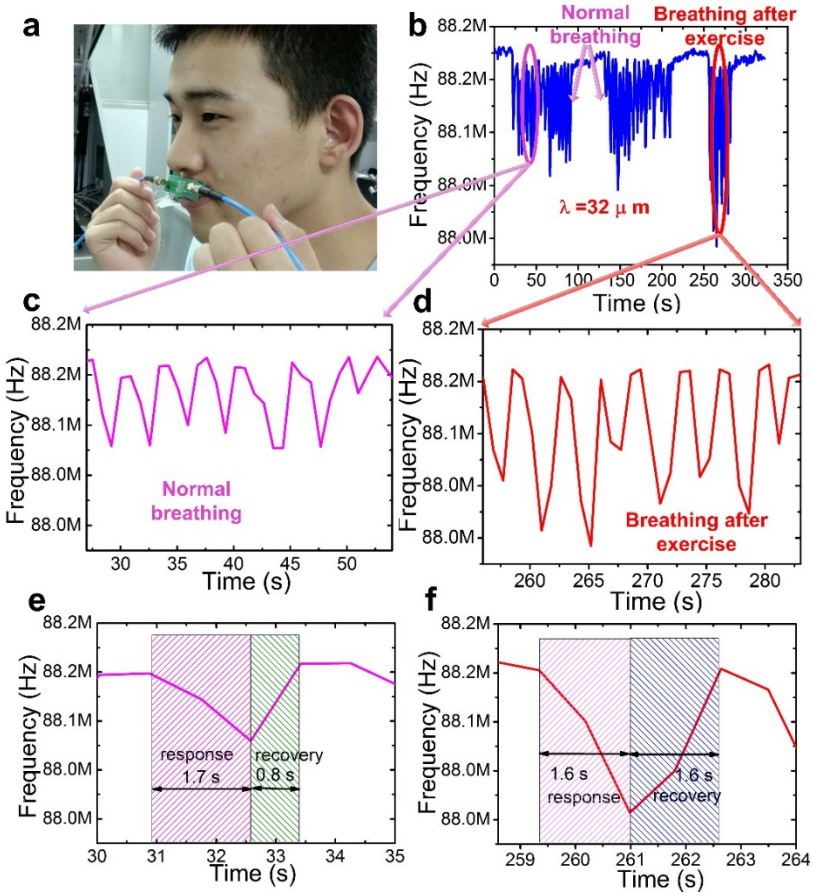

Figure 10. (a) The sensor was placed near the nose and responded to the respiration; (b) Resonant frequency shift of the transparent SAW sensor with breathing for normal state and state after exercise; (c)&(d) Enlarged figure for resonant frequency shift for normal state and state after exercise; (e)The response and recovery times of the transparent SAW sensor are about 1.7 s and 0.8 s for the volunteer's normal respiratory. The total response time for one cycle is about 2.5 s, shorter than the breathing period of ~3.75 s; (f) The response and recovery times of the transparent SAW sensor are about 1.6 s and 1.6 s for volunteer's respiratory after exercise. The total response time for one cycle is about 3.2 s, shorter than the breathing period of ~3.3 s.

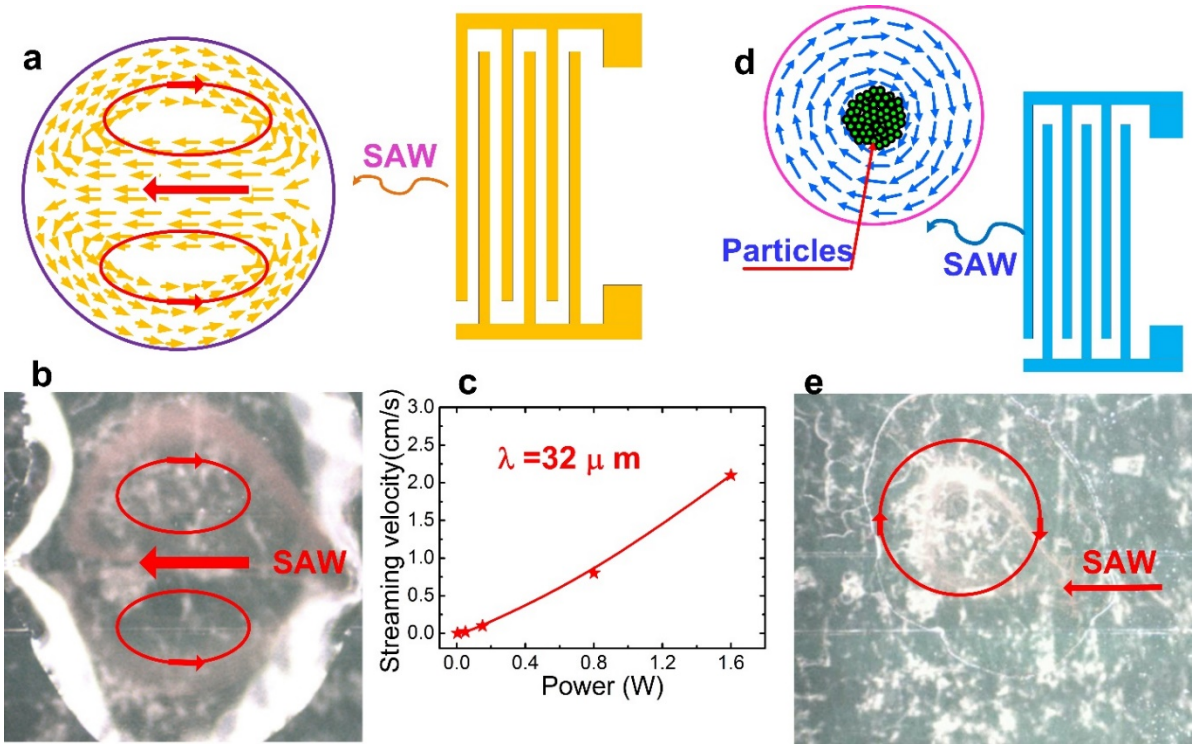

Figure 11. (a) Schematic drawing of acoustic streaming inside a liquid droplet, (b) snapshot of acoustic streaming induced by transparent SAW device, showing double vortex patterns. The red arrow indicates the SAW direction entering the liquid. (c) The effect of RF power on the streaming velocity, showing rapid increase in streaming velocity with RF power at droplet size of 2 μL; (d) A schematic drawing to show circulating streaming and particle concentration induced by SAW off the central wave path; (e) image of circulating streaming and particle concentration in the droplet after applying a RF signal power of 1.6 W at droplet size of 2 μL.